ACADEMIA MATERIALS SCIENCE

Research Article
Published: 2024-06-25
https://doi.org/10.20935/AcadMatSci6240

Silver-blend hydroxyapatite bio-ceramics for enhanced photocatalytic degradation of methylene blue

Manoj V. Junnarkar[1], Prateek V. Sawant[1], Mahadev A. Parekar[1], Avadhut V. Kardile[1], Ashish B. Thorat[2], Ramakant P. Joshi[1], Ravindra U. Mene[1,*]

Academic Editor(s): Ricardo Faria Ribeiro and Raul D.S.G. Campilho

Abstract

In this article, nanostructured hydroxyapatite (HAp) and Ag-doped HAp are synthesized via a wet chemical precipitation route and ion-exchange methods to analyze their photocatalytic performance via the degradation of organic dyes. X-ray diffraction (XRD), Fourier-transform infrared spectroscopy (FTIR), and scanning electron microscope (SEM)/energy-dispersive X-ray spectroscopy (EDS) are used to analyze the structural, functional, morphological, and elemental properties of the samples. Ultra violet (UV)-visible diffuse reflectance spectroscopy is used to monitor the changes in the band-gap energies of the samples. The Tauc plots show the decrease in the band gap of HAp due to Ag doping. XRD confirms the crystalline hexagonal phase of HAp, whereas the SEM and EDS further confirm the presence of Ag ions in the HAp matrix. FTIR spectra validate the characteristic bands of hydroxyl and phosphate species of HAp. The degradation of organic dyes through photocatalysis was carried out using pure and Ag-doped HAp samples as the catalysts under solar irradiation. It is observed that the Ag-HAp photocatalysts show a better efficiency toward the degradation of methylene blue (MB) compared to malachite green or Rhodamine B. HAp sample with Ag (0.15 M) content showed a remarkable degradation of MB (97% in 60 minutes) when compared to pure HAp, which showed only 11% degradation. The effect of Ag doping on the reaction kinetics was also studied, wherein the reaction rates were enhanced by increasing Ag concentrations. Moreover, the Ag-doped HAp shows excellent recycling ability highlighting its practical usage as a photocatalyst for wastewater treatment.

Keywords: *Bio-ceramic, hydroxyapatite (HAp), chemical precipitation, ion exchange, methylene blue, photocatalysis*

Citation: Junnarkar MV, Sawant PV, Parekar MA, Kardile AV, Thorat AB, Joshi RP, Mene RU. Silver-blend hydroxyapatite bio-ceramics for enhanced photocatalytic degradation of methylene blue. *Academia Materials Science* 2024;1. https://doi.org/10.20935/AcadMatSci6240

1. Introduction

Photocatalysis has emerged as a crucial technology in addressing environmental challenges, particularly in the realm of wastewater treatment. One of the major contaminants in water is organic dyes such as methylene blue (MB), used in textile industries [1]. These organic dyes are highly water soluble and pose a threat to humans and the environment due to their toxicities [2]. In particular, traces of MB in aquatic environments attenuate the penetration of light and oxygen, limiting the photosynthesis process in aquatic plants and, in turn, misbalancing the aquatic ecosystem [3–5]. Moreover, exposure to or ingestion of MB may cause nausea, skin coloration, vomiting, diarrhea, cyanosis, and many other health conditions in humans [6–8]. Therefore, it is of utmost importance to treat industrial wastewater before its release into the environment. Traditional methods such as filtration and dilution for degrading the pollutants often suffer from inefficiency and environmental drawbacks [9, 10]. Photocatalysis offers a sustainable alternative by harnessing the power of light to drive chemical reactions for the degradation of organic dyes and other harmful compounds. This process relies on semiconductor photocatalysts, which upon absorption of photons generate electron-hole pairs capable of initiating redox reactions, ultimately breaking down organic pollutants into harmless byproducts [11].

Hydroxyapatite (HAp) has emerged as a promising photocatalyst among a plethora of available semiconductor materials such as TiO_2 [12], ZnO [13], etc., due to its inherent biocompatibility, low toxicity, and excellent chemical stability [14]. Thus, for environmental applications wherein the potential release of toxic byproducts must be minimized, HAp becomes an attractive candidate. Additionally, HAp can be easily synthesized using cost-effective methods, further enhancing its appeal for large-scale implementation in photocatalytic processes [15]. The earliest documented investigation on pure HAp as a photocatalyst was conducted by Nishikawa and Omamiuda in 2002 [16]. The authors carried out the photodegradation of methyl mercaptane under UV radiation using HAp as the photocatalyst. However, pure defect-free HAp is known to be an insulating material having a very wide band gap of 6 eV [17]. Due to this, defect-free

[1]Department of Physics, PDEA's Annasaheb Magar Mahavidyalaya, Hadapsar, Pune, Maharashtra 411028, India.
[2]Department of Physics, Savitribai Phule Pune University, Pune, Maharashtra 411007, India.
*email: drmeneravindra@pdeaamcollege.edu.in; ravimeneamm@gmail.com

HAp may not show any photocatalytic activity. A subsequent study by Nishikawa showed that the heat treatment of HAp at 200°C altered the phosphate groups in the material, resulting in imperfections in its lattice structure. These defects then trapped the generated reactive oxygen species leading to the photocatalytic activity of the material [18]. Subsequently, numerous studies were reported that employed HAp as a photocatalyst to degrade a wide range of organic and inorganic pollutants. A study by Tripathi et al. described the effect of surface modifications on the photocatalytic activity of HAp, wherein the HAp nanofibers synthesized using yeast extract were employed as photocatalysts for the efficient degradation of MB [19]. According to Tanaka et al., the first step in the photodegradation of dimethyl sulfide was its adsorption on the P–O–H groups, describing the pivotal role of phosphate groups in the degradation mechanism [20]. Piccirillo et al. reported their study on HAp derived from calcium acetate-treated cod fish bones. The photocatalytic activity of the samples was hypothesized to result from the formation of oxygen vacancies in the HAp lattice during the calcination phase [21].

However, most of the studies on pristine HAp as a photocatalyst show a high degree of inefficiency primarily due to the wide band gap of HAp. Thus, doping HAp with metals or other photocatalytic materials could lead to a reduction in the band-gap energy and increase the efficiency of the photodegradation process. A study by Liu et al. concluded that a TiO_2/HAp composite containing 2.5% Ti exhibited tenfold more degradation of methyl orange than pure HAp [22]. Similarly, Golshan et al. showed that under optimal pH and radiation conditions, the Fe_3O_4@HAp composite had a removal efficiency of 97% toward acid red dye, which was three times more when compared to degradation carried out under normal conditions [23]. Othmani et al. demonstrated that doping HAp crystals with copper atoms altered the crystal structure and surface area of HAp. The photocatalytic degradation efficiency of the material toward naphthol blue black dye increased from 20% to 40% when the Cu content was raised from 0.5 to 1.5 at.% after 30 minutes of radiation [24]. Mondal et al. reported that Au-loaded HAp nanoparticles degrade MB when exposed to visible light. The authors attributed this to electron production caused by radiation-induced Au excitation [25].

Motivated by the promising outcomes reported in the above-mentioned studies, we herein attempt to study the impact of silver doping on the photocatalytic performance of HAp nanoparticles. The Ag-doped HAp nanoparticles are synthesized via the chemical precipitation method at varying concentrations of Ag. The samples are characterized via X-ray diffraction (XRD), FTIR, filed emission scanning electron microscopy (FE-SEM), and UV-visible diffuse reflectance spectroscopy (UV-DRS) to investigate the structural, morphological, and optical changes in the HAp lattice brought about by Ag doping. Furthermore, the photocatalytic performance of the samples is assessed using MB, malachite green (MG), and Rhodamine B (RhB) as model organic pollutants undergoing degradation. The radical trapping experiments were performed to detect the active species during the photocatalysis process. Considering the insights gained during the studies, a plausible mechanism of dye degradation by Ag-HAp is proposed.

2. Materials and methods

2.1. Chemicals and reagents

The starting precursors for calcium and phosphate (>98% pure, Loba Chemicals, Mumbai, India) are calcium nitrate tetrahydrate ($Ca(NO_3)_2{\cdot}4H_2O$) and di-ammonium hydrogen orthophosphate ($(NH_4)_2{\cdot}HPO_4$). The reagents also include silver nitrate ($AgNO_3$) and ammonium hydroxide (NH_4OH) to adjust pH values. MB, MG, and RhB were used as model pollutants for the degradation process. Isopropyl alcohol (IPA) and disodium ethylenediaminetetraacetic acid (EDTA-2Na) were used as radical scavengers. All of the reagents are of analytical grade and were used as received without further purification.

2.2. Synthesis of pure and Ag-doped HAp

As mentioned in earlier literature, the wet chemical precipitation method was used to synthesize pure HAp [26]. Calcium nitrate tetrahydrate ($Ca(NO_3){\cdot}4H_2O$) and di-ammonium hydrogen orthophosphate ($(NH_4)_2{\cdot}HPO_4$) were used as starting precursors. The calcium and phosphorus molar concentrations were adjusted to have a theoretical Ca/P ratio of 1.67. The precipitation process was carried out with 1 M of calcium nitrate tetrahydrate solution by the drop-wise addition of 0.6 M of di-ammonium hydrogen orthophosphate. The ammonia solution was used to adjust the pH to 10 of the reaction mixture, along with continuous stirring at 100°C for three hours. After the reaction, the reaction mixture was aged for 24 hours. Using double-distilled water, white precipitates were washed three to four times and dried in an air oven at 100°C overnight. Finally, the product was ground to a fine powder and annealed in a muffle furnace at 800°C for two hours. The chemical reaction for the process is given as [27]:

$$10Ca(NO_3)_2\cdot 4H_2O + 6(NH_4)_2HPO_4 + 2NH_4OH \rightarrow Ca_{10}(PO_4)_6(OH)_2 + 20NH_4NO_3 + 46H_2O \quad (1)$$

The synthesis of $[(Ca_{10-x}Ag_{2x})(PO_4)_6(OH)_2]$ with x = 0.05, 0.10, and 0.15 M was carried out via an ion-exchange process as reported in earlier works [27–29]. Briefly, 0.05 M, 0.10 M, and 0.15 M solutions of $AgNO_3$ were prepared in 50 mL of double-distilled water. Then, 1 g of HAp was added to this solution and kept on a rotating shaker for six hours at 120 rpm. After the ion-exchange process, excess water was decanted and the samples were dried at 100°C for 12 hours. The samples were labeled 0.05 Ag-HAp, 0.10 Ag-Hap, and 0.15 Ag-HAp, respectively. The synthesis of Ag-HAp can be summarized via the following equation [27].

$$Ca_{10}(PO_4)_6(OH)_2 + 2xAg \rightarrow 2Ca_{10-x}Ag_{2x}(PO_4)_6(OH)_2 + xCaO \quad (2)$$

2.3. Characterization techniques

XRD, scanning electron microscope (SEM), Fourier-transform infrared spectroscopy (FTIR), and UV-DRS were utilized to identify the structural properties, surface morphology, functional groups, and optical properties of pure and doped Ag-HAp. Bruker AXS Germany (Model D8 Advanced, Berlin, Germany) with Cu Kα (l = 1.5405 Å) incident radiation is used to record the XRD pattern in the 2θ range of 20°–60°. The elemental analysis and surface morphology are visualized using an SEM (FE-SEM Hitachi S-4800, Hitachi, Japan). FTIR spectroscopy (Shimadzu,

Nakagyō-ku, Japan) is used to determine the functional group in the frequency range 400–2,000 cm^{-1}. The UV-DRS analysis was also conducted using Shimadzu, Model UV-2600, Kyoto, Japan.

2.4. Photocatalytic measurement

The photocatalytic experiments were carried out using MB, MG, and RhB as model pollutants. First, the desired dye was dissolved in deionized water to a concentration of 100 ppm. This stock solution was further diluted to 10 ppm, 100 mL of which was used to carry out the degradation experiment. A catalyst dose of 100 mg was dropped in this dye solution and the reaction mixture was irradiated under sunlight (intensity of 624 W/m^2 or 79,000 lux). After specific time intervals, the aqueous solution of the dye was sampled and centrifuged to remove the photocatalysts, and the existing dye concentration was measured using a UV-Vis spectrophotometer (PerkinElmer Lambda 265, Waltham, MA, USA).

The decolorization efficiency (%) was calculated by the following equation:

$$\text{Decolorization}(\%) = \frac{C_0 - C}{C_0} \times 100 \quad (3)$$

where C_0 and C represent, respectively, the initial concentration and the concentration at any time t of the MB solution during the photodegradation experiment [30]. The recycling ability and scavenger studies have also been performed, which are discussed in subsequent sections.

3. Results and discussion

3.1. XRD studies

Figure 1a–d shows XRD plots of pure and Ag-doped HAp samples. The Joint Committee on Powder Diffraction Standards (JCPDS) XRD card (09-432) is used to identify the XRD phase of HAp. The crystalline hexagonal phase of HAp is confirmed by the presence of all characteristic peaks at the 2θ values 25.6°, 26.4°, 28.5°, 29.1°, 30.1°, 31.8°, 33.2°, 35.3°, 36.1°, 37.9°, 40.1°, 43.5°, 44.2°, 45.5°, 46.8°, 49.6°, 52.7°, 56.4°, and 57.6°. As observed, the intensities of the characteristic peaks between 2θ = 25° and 35° dropped as the doping concentration of Ag was increased. This may indicate a drop in crystallinity due to the crystal imperfections introduced by Ag ions. Moreover, a slight broadening of the most intense peak corresponding to the crystal plane (3 0 1) is also observed, which may be attributed to lower crystallite sizes and micro-strains induced by Ag doping [31]. This was confirmed by calculating the average crystallite sizes using the Scherrer equation.

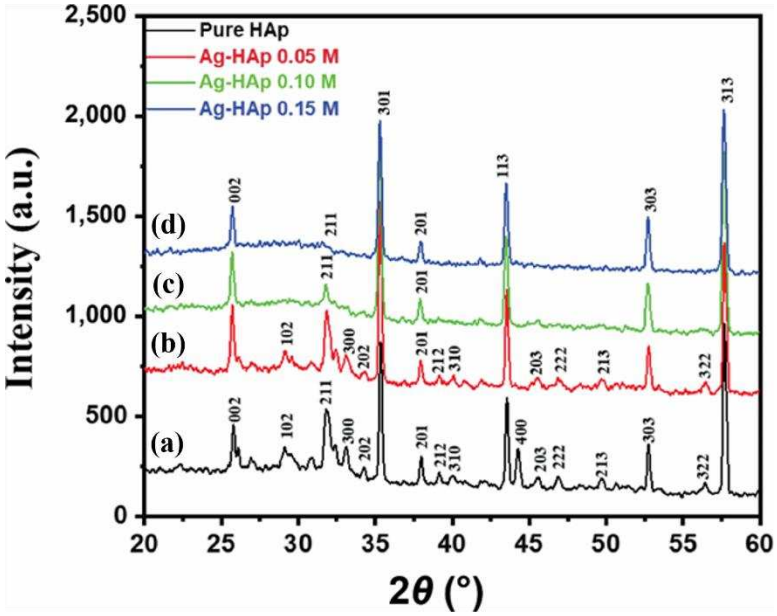

Figure1 • XRD analysis of the synthesized samples: (a) pure HAp, (b) 0.05 Ag-HAp, (c) 0.10 Ag-HAp, and (d) 0.15 Ag-HAp.

3.2. Scanning electron microscopy

Figure 2a and **2b** FE-SEM images show the aggregation of smaller spherical particles in both pure and 0.15 Ag-HAp samples. The entire surface is covered in uniformly sized grains, with the majority of the particle sizes falling in the range of approximately 100–300 nm, as seen in the size distribution histogram. **Figure 2c** illustrates the energy-dispersive X-ray spectroscopy (EDS) investigation of the 0.15 Ag-HAp sample. The primary groups identified in the EDS spectra are calcium and phosphate. Moreover, the silver concentration of 1.56 at.% suggests the successful integration of Ag ions in the HAp matrix.

3.3. Fourier-transform infrared spectroscopy

Figure 3 displays the FTIR spectra of pure and Ag-doped HAp (0.05 M, 0.10 M, and 0.15 M) within the wave number range of 1,600–400 cm^{-1}. The spectra showed the distinct bands of hydroxyl and phosphate species confirming the HAp structure. The characteristic of a well-crystallized apatite phase was described by peaks in the regions 450–650 cm^{-1} and 950–1,100 cm^{-1} [32]. The bands are present at 1,030 cm^{-1} (ν_3), and 1,075 cm^{-1} (ν_3) to the asymmetric ν_3 (P–O) stretching. Moreover, the band at 550 cm^{-1} is associated with the triply degenerated ν_4 vibration of the O–P–O bond, and the bands at 499 cm^{-1} are related to the doubly degenerated ν_2 bending of O–P–O bond. The peak 926 cm^{-1} for internal modes of the PO_4^{3-} tetrahedral ν_1 frequency corresponds to the symmetric stretching of P–O bonds. The bands located in between 900 cm^{-1} and 1,300 cm^{-1} describe PO_4^{3-} bands [27, 33, 34]. The characteristic peaks observed at 533 cm^{-1} describe –OH stretching vibrations modes [35]. The peak at 721 cm^{-1} (ν_4) refers in-plane deformation O–C–O bending modes in the CO_3 group [36].

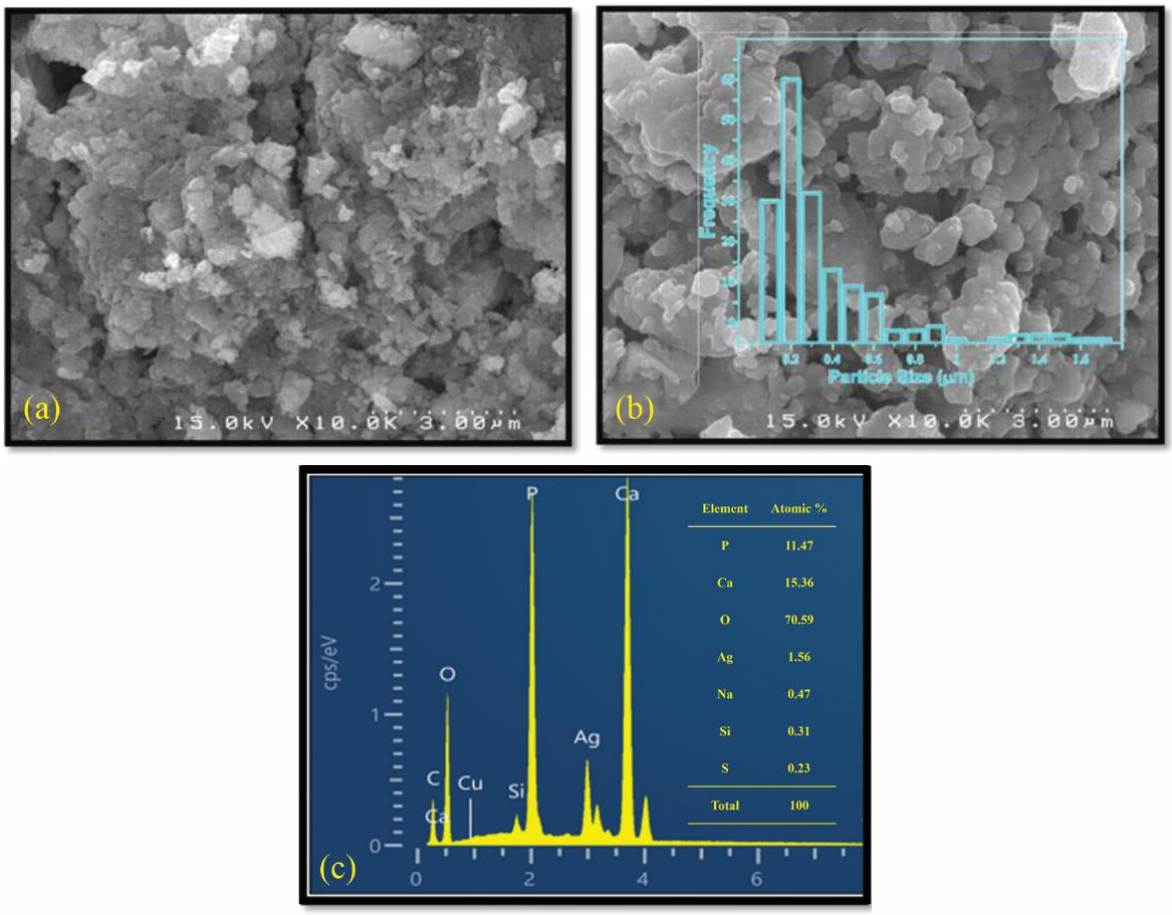

Figure 2 • FE-SEM image of the synthesized (a) pure HAp, (b) 0.15 Ag-HAp with size distribution histogram, and (c) EDS of 0.15 Ag-HAp.

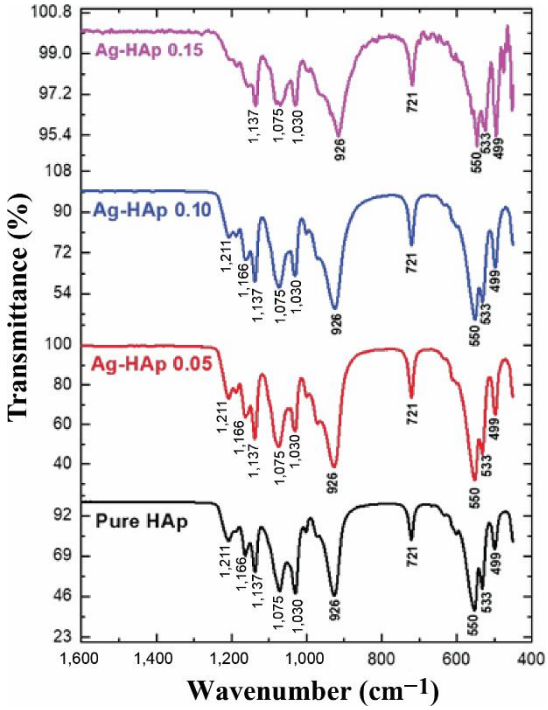

Figure 3 • FTIR spectra of pure HAp, 0.05 Ag-HAp, 0.10 Ag-HAp, and 0.15 Ag-HAp.

3.4. UV-Vis spectroscopy

UV-DRS was employed to investigate the optical properties and band-gap energies of the photocatalyst samples. **Figure 4a** and **4b** presents the UV-DRS spectra of the pure HAp and Ag-HAp catalysts, respectively. The absorption edge observed in the spectra corresponds to the transition of electrons from the valence band (VB) to the conduction band (CB). A slight red shift of the absorption edge was observed indicating a reduction in the band-gap energy (E_g). The band-gap energy was calculated by plotting the Kubelka-Munk function against the photon energy (Tauc plot) and determining the intercept of the tangent to the plot at the absorption edge. The corresponding Tauc plots for pure HAp and 0.15 Ag-HAp are shown in **Figure 4c** and **4d**, respectively. The band-gap energy for pure HAp was calculated to be approximately 5.3 eV, which is consistent with its known wide band gap. This limits its photocatalytic activity to a great extent. In contrast, the 0.15 Ag-HAp photocatalyst exhibited a band-gap energy of approximately 3.19 eV. This significant reduction in the band gap energy due to Ag doping enhances the light absorption ability of the material, thus enhancing its photocatalytic activity.

3.5. Photocatalytic activity

3.5.1. Degradation of methylene blue

Using UV-Vis spectroscopy, the photocatalytic degradation of MB was investigated, monitoring the decrease in the peak absorbance value at λ_{max} = 664 nm. **Figure 5a–d** represents the absorption spectra for the photocatalytic degradation of MB over time via pure and Ag-doped HAp as the photocatalysts. The degradation of MB with respect to the residual concentration over time is represented in **Figure 6a** and the percentage degradation with time is visualized in **Figure 6b**. MB solution irradiated without the presence of any catalyst shows merely ~4% degradation in 60 minutes. In the presence of a pure HAp catalyst, the degradation efficiency slightly increased to ~11%. However, the Ag-doped HAp photocatalysts show a remarkable

degradation of up to 97% in the same time frame for Ag-HAp (0.15 M). It is also obvious that with an increase in Ag-doping concentrations, the photocatalytic activity of HAp is enhanced. **Table 1** shows a comparison of various HAp composites from previous studies and the present study. It can be inferred that Ag-doped HAp can function as a fairly efficient photocatalyst for organic dye degradation.

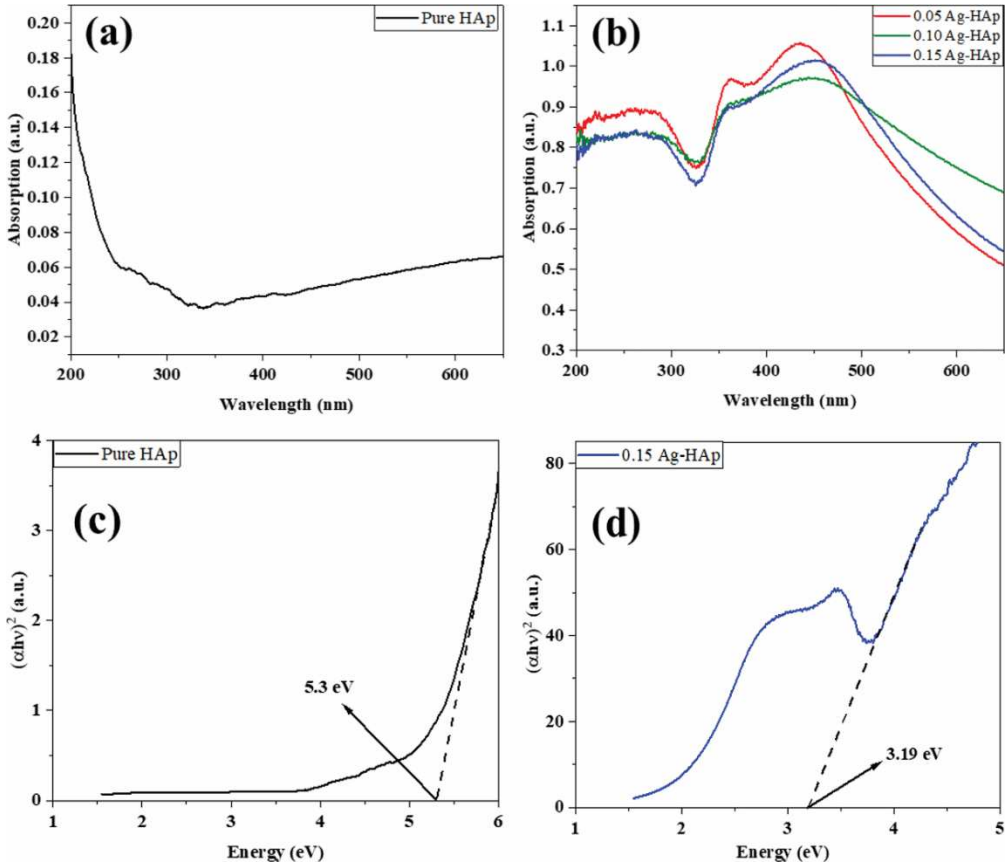

Figure 4 • UV-Vis absorption spectra of (a) pure HAp and (b) Ag-doped HAp and the corresponding Tauc plots for (c) pure HAp and (d) 0.15 Ag-HAp.

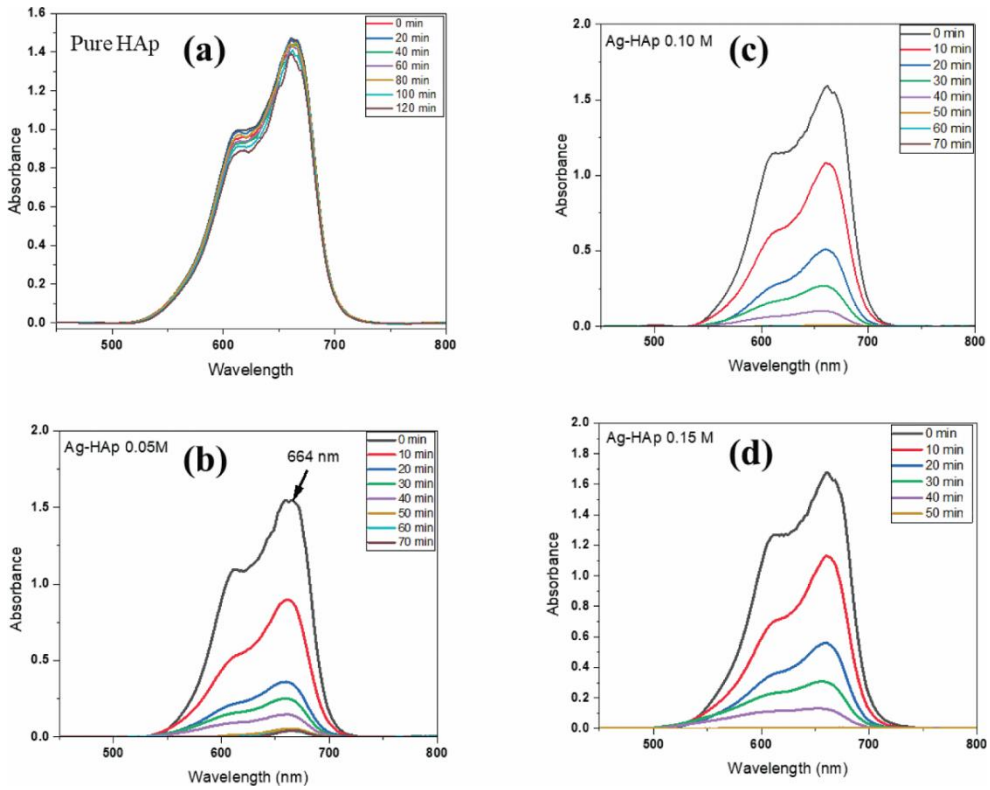

Figure 5 • Time-dependent absorption spectra of MB during photocatalytic degradation via (a) pure HAp, (b) Ag-HAp 0.05 M, (c) Ag-HAp 0.10 M (d), and Ag-HAp 0.15 M.

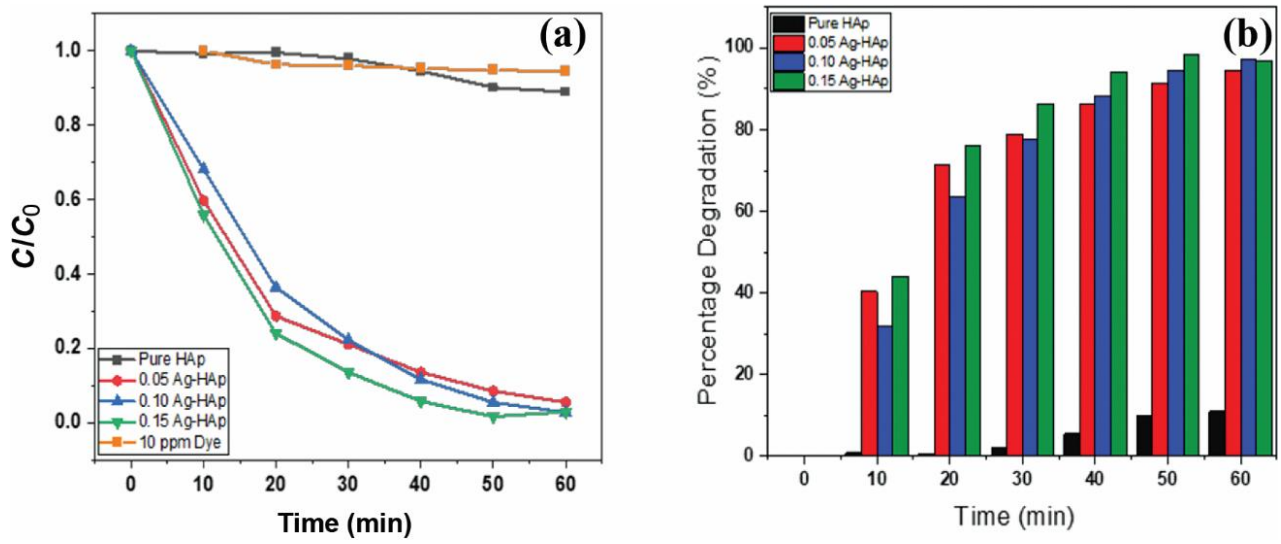

Figure 6 • (a) Methylene blue (MB) degradation with respect to time for different catalysts and (b) percentage degradation of MB at specific time intervals.

Table 1 • Comparison of photocatalytic activities of various hydroxyapatite composites

HAp composite	Dye	Time	Efficiency (%)	Ref.
Ag_3PO_4/HAp-3 (14.6 wt.% of Ag)	Methylene blue	120 min	70.30	[37]
HAp/g-C_3N_4	Methylene blue	100 min	93.69	[38]
0.8Ag/Fe-HAp@CA	Methylene blue	2 h	>90	[39]
Ag-HAp (0.1 M silver nitrate + 0.1 M calcium nitrate)	Crystal violet	90 min	64	[40]
0.63Cu_HAp (0.63% copper doping level in HAp)	Congo red	180 min	99	[41]
HAp/Ta core-shell nanorods	Turq blue GL	8 h	99	[42]
ZP14 (ZnO:NHAp ratios 1:4)	Methylene blue	<100 min	91	[35]
Ag_3PO_4/HAp-2 (with a nominal silver loading of 12.7%)	Methylene blue	120 min	98	[43]
Au–HAp (loaded with 0.055 wt.% Au)	Methylene blue	9 h	32.47	[25]
Ti-HAp-0.2, 0.20 mole ratios for Ti/(Ca + Ti)	Methyl orange	2 h	98.9	[44]
Nanostructured hydroxyapatite spheres	Methylene blue	240 min	74.75	[45]
HAp/11 wt.%Ti	Methylene blue	8 h	Complete discoloration	[46]
1:1-Ag_3PO_4/AgBr/HAp	Methylene blue	40 min	97.63 (complete degradation)	[47]
HAp-sodium alginate	Methylene blue	30 min	79.9	[48]
HAp-Ag_3PO_4	Sunfix red	45 min	100	[49]
Ag-HAp 0.15	Methylene blue	70 min	97	Present work

The photodegradation process obeys the pseudo-first-order reaction kinetics model represented by the following equation:

$$r = -\frac{dc}{dt} = \frac{k'KC}{1+KC} \quad (4)$$

Where r is the degradation rate expressed in (mol·L^{-1}·min^{-1}), C is the concentration of pollutant dye (MB) solution, k' is the reaction rate constant, and K is the adsorption equilibrium constant. If the concentration of pollutant dye is low the $KC << 1$ then the reaction can be expressed as,

$$-\frac{dc}{dt} = k'KC \quad (5)$$

$$-\frac{dc}{dt} = kC \quad (6)$$

where $k = k'K$ is the rate constant of pseudo-first-order reaction. The logarithmic form of the equation is:

$$\ln\left(\frac{C}{C_o}\right) = -kt \quad (7)$$

where C_0 is the initial concentration of the dye, C is the concentration of the dye at different times, t is the irradiation time (minutes), and k is the rate constant [50]. The slope of the ln C/C_0 versus time provides the rate constant. **Figure 7a** shows the linear fits of pseudo-first-order reaction kinetics and a comparison of reaction rate constants is visualized in F**igure 7b**. As evident from the kinetics study, the reaction rate of MB degradation over HAp catalysts increased with an increase in Ag-doping concentrations. Pure HAp degraded MB with a low reaction rate of 0.00167 min^{-1}, whereas 0.15 M Ag-doped HAp photocatalyst showed an increased degradation rate of 0.06828 min^{-1}. The photocatalytic study clearly underlines the role of Ag doping in enhancing the photocatalytic degradation efficiency of HAp. The comparison of reaction rate constants for the Ag-doped HAp photocatalysts is given in **Table 2**.

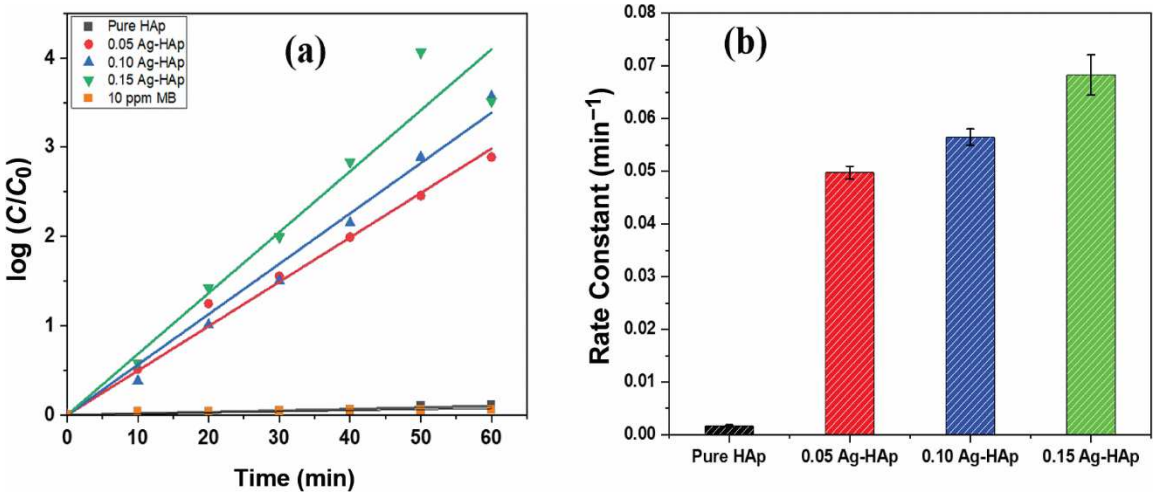

Figure 7 • (a) Linear fit of pseudo-first-order reaction kinetics and (b) comparison of reaction rate constants for different samples.

Table 2 • Comparison of the reaction rate constants for the HAp photocatalysts

Catalyst	Reaction constant (min^{-1})	Standard deviation
Pure HAp	0.00167	0.00021
0.05 Ag-HAp	0.04974	0.0012
0.10 Ag-HAp	0.05644	0.00156
0.15 Ag-HAp	0.06828	0.0038

3.5.2. Effect of various dyes

The comparative degradation experiments were conducted using MB, RhB, and MG dyes to investigate the photocatalytic degradation efficacy of 0.15 Ag-HAp as a catalyst. **Figure 8a** illustrates the percentage degradation of these dyes after 60 minutes of irradiation. The Ag-HAp catalyst achieved a degradation of approximately 44.6% for MG and 16.6% for RhB, which were both lower compared to MB, which showed a degradation of 96.8%. These results indicate that the Ag-HAp catalyst exhibits a higher degradation efficiency for MB compared to MG and RhB. This preferential degradation is further supported by the reaction rate analysis presented in **Figure 8b**, which validates the superior catalytic performance of Ag-HAp in MB degradation.

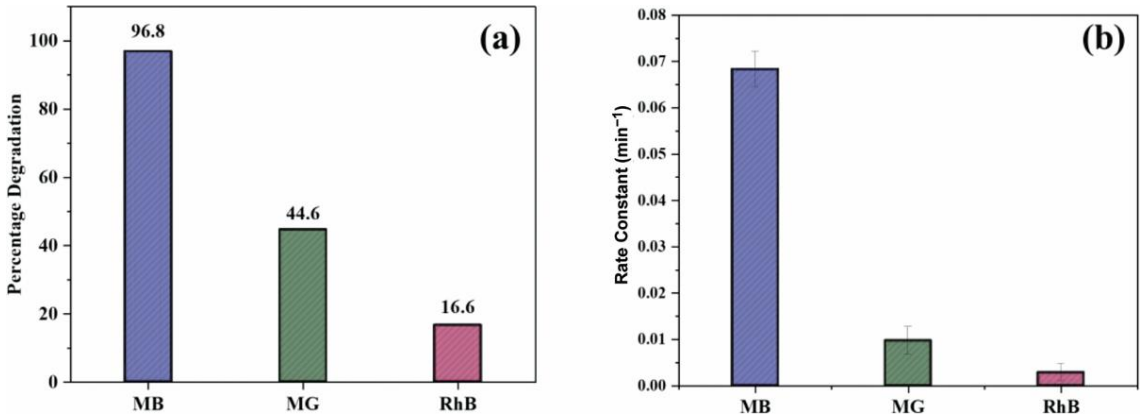

Figure 8 • (a) Percentage degradation of various dyes after 60 minutes of irradiation and (b) comparison of reaction rates of the different dyes.

3.5.3. Scavenger studies and recyclability

The scavenger studies were carried out using IPA and disodium ethylenediaminetetraacetic acid (EDTA.2Na) for (OH•) and holes (h+) species, respectively [51]. The results are depicted in **Figure 9a**. Due to the effect of EDTA scavenger, the photocatalytic activity of 0.15 Ag-HAp is greatly suppressed. However, with the addition of IPA, the photocatalytic efficiency of the material remained unaffected. Thus, we concluded that holes (h+) are major contributors to the photodegradation of MB. To evaluate the recyclability of the 0.15 Ag-HAp photocatalyst, cyclic degradation experiments were performed. In each cycle, the photocatalyst was utilized to degrade MB, followed by recovery, washing, and drying for subsequent reuse. After each degradation experiment, the Ag-HAp photocatalyst was collected by centrifugation, washed thoroughly with deionized water to remove any residual dye molecules, and then dried overnight at 100°C. This revived photocatalyst was then subjected to a new cycle of MB degradation under the same conditions. The results of the recyclability tests are shown in **Figure 9b**. The degradation efficiency of the photocatalyst for the target dye was recorded over four consecutive cycles. Initially, the catalyst showed a high degradation efficiency of 94.35%. After the first cycle, a slight decrease in efficiency was observed, with the degradation efficiency stabilizing around 90% by the fourth cycle.

These results demonstrate that the 0.15 Ag-HAp photocatalyst retains a significant portion of its photocatalytic activity even after multiple cycles of reuse. The minor reduction in efficiency can be attributed to the potential loss of catalyst and thus reduction in active sites [52, 53]. Nevertheless, the high retention of photocatalytic activity over several cycles underscores the potential of Ag-HAp as a durable and reusable photocatalyst for dye degradation.

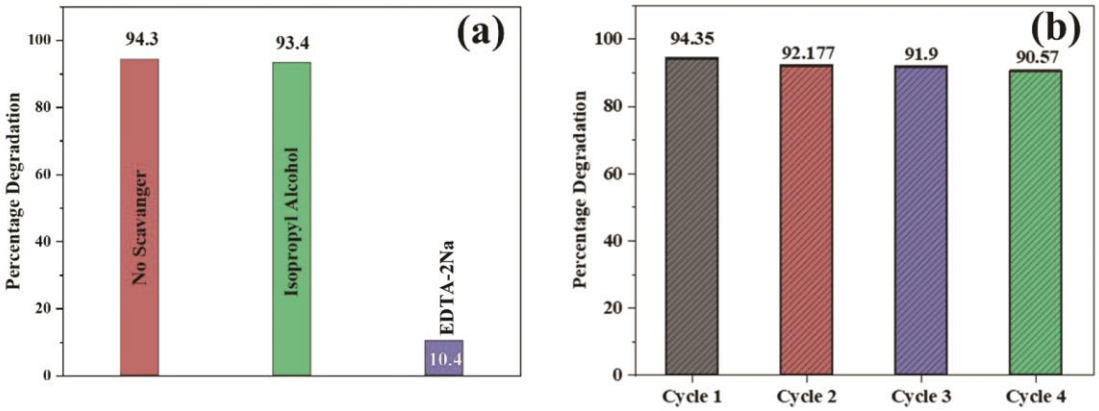

Figure 9 • (a) Percentage degradation of MB in the presence of various scavengers and (b) percentage degradation of MB over four cycles of reusing the Ag-HAp photocatalyst.

3.6. Degradation mechanism

The mechanism of the photocatalytic degradation process is illustrated schematically in **Figure 10**. When the catalyst surface is irradiated with light, photons with energy greater than the band-gap energy of HAp excite the electrons in the VB [54]. The excited electrons migrate to the CB of HAp, leaving holes in the VB. The introduction of Ag in the HAp lattice creates lattice imperfections, which act as electron-trapping sites. Furthermore, the fermi energy of Ag lies lower than the CB of HAp, creating an extra energy level between the VB and the CB, thereby reducing the band gap from 5.3 to 3.19 eV [55]. Due to this band alignment, electrons from the CB migrate to the Ag nanoparticles. Under light irradiation, the Ag nanoparticles show a localized surface plasmon resonance (LSPR) effect. The electron entrapment effect of the LSPR not only increases light absorption but also significantly reduces charge recombination [56].

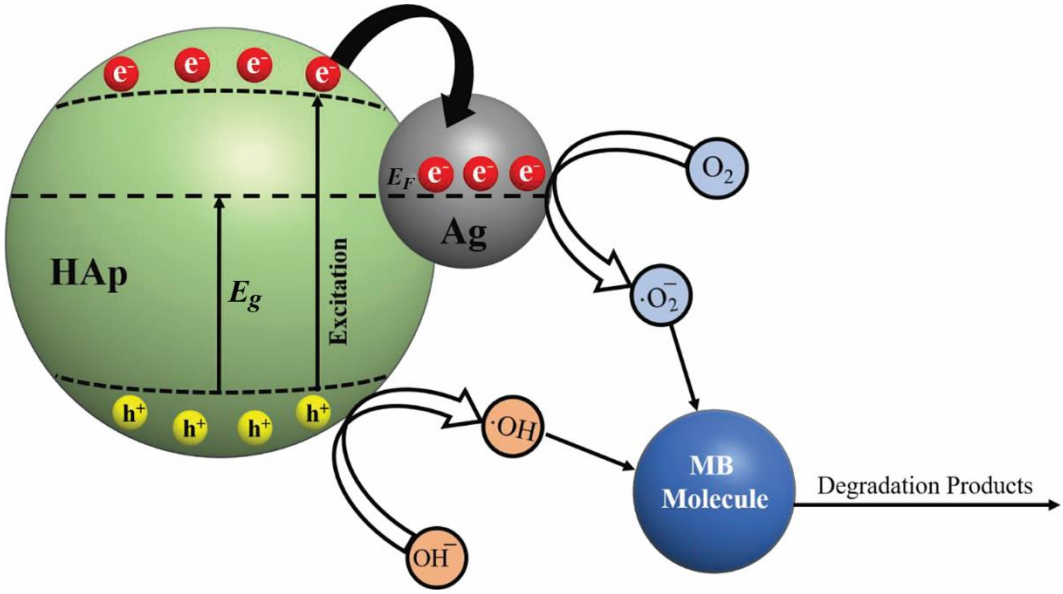

Figure 10 • Schematic representation of the mechanism of photocatalytic degradation of MB using Ag-doped HAp as the photocatalyst.

These electrons can now be seized by surface oxygen-producing superoxide radicals (•O_2). By interacting with (OH–) ions, the holes in the VB generate hydroxyl radicals (•OH) [57]. These superoxide and hydroxyl radicals can then attack the MB molecules via a series of redox reactions, degrading the pollutant in the process. The degradation process can be summarized by the following chemical reactions.

$$Ag-HAp+h\nu \rightarrow e^-_{CB} + h^+_{VB} \quad (8)$$

$$e^-_{CB} + O_2 \rightarrow \bullet O^-_2 \quad (9)$$

$$h^+_{VB} + OH^- \rightarrow \bullet OH \quad (10)$$

$$\bullet O^-_2 + \bullet OH + MB \rightarrow \text{Degradation products} \quad (11)$$

The role of Ag in reducing the band gap and, in turn, enhancing the photocatalytic activity of HAp is clearly underlined in the degradation mechanism.

4. Conclusions

This article reveals the role of silver ions in enhancing the photocatalytic efficiency of HAp bio-ceramic. The analytical tools, such as XRD, FE-SEM, FTIR, and UV-DRS, were used to clarify the similarities and differences between pure and Ag-doped HAp. The hexagonal HAp phase was identified using the XRD pattern and no phase changes were detected due to the presence of Ag. Also, the band gap of HAp was significantly reduced due to Ag doping. The FTIR spectra confirm the presence of all the characteristic bands corresponding to pure HAp. The photocatalytic performance of the samples was assessed via the degradation of model pollutants in MB, MG, and RhB. The 0.15 Ag-HAp sample showed a remarkably higher degradation efficiency for MB compared to MG and RhB. The effect of Ag doping on the reaction kinetics was also studied, wherein the reaction rates were enhanced by increasing Ag concentrations. The Ag-HAp photocatalyst shows a consistent performance over multiple cycles of reuse, making it a promising photocatalyst for wastewater treatments.

Acknowledgments

The authors would like to acknowledge PDEA's Annasaheb Magar Mahavidyalaya, Hadapsar, Pune, for providing research facilities.

Funding

The authors declare no financial support for the research, authorship, or publication of this article.

Author contributions

Conceptualization, R.U.M.; methodology and experimentation, M.V.J. and M.A.P.; analysis, A.V.K.; writing—original draft, P.V.S.; writing—review and editing, R.P.J. and A.B.T. All authors have read and agreed to the published version of the manuscript.

Conflict of interest

The authors declare no conflict of interest.

Data availability statement

Data supporting these findings are available within the article, at https://doi.org/10.20935/AcadMatSci6240, or upon request.

Institutional review board statement

Not applicable.

Informed consent statement

Not applicable.

Sample availability

The samples used in this study are available in the Research Laboratory of PDEA's Annasaheb Magar Mahavidyalaya, Hadapsar, Pune.

Additional information

Received: 2024-03-30

Accepted: 2024-06-04

Published: 2024-06-25

Academia Materials Science papers should be cited as *Academia Materials Science 2024*, ISSN 2997-2027, https://doi.org/10.20935/AcadMatSci6240. The journal's official abbreviation is *Acad. Mat. Sci.*

Publisher's note

Copyright

References

1. Abd-Elhamid AI, Emran M, El-Sadek MH, El-Shanshory AA, Soliman HMA, Akl MA, et al. Enhanced removal of cationic dye by eco-friendly activated biochar derived from rice straw. Appl Water Sci. 2020;10:1–11.
2. Benkhaya S, M'rabet S, El Harfi A. A review on classifications, recent synthesis and applications of textile dyes. Inorg Chem Commun. 2020;115:107891.
3. Makeswari M, Saraswathi P. Photo catalytic degradation of methylene blue and methyl orange from aqueous solution using solar light onto chitosan bi-metal oxide composite. SN Appl Sci. 2020;2:1–12.
4. Cheng J, Zhan C, Wu J, Cui Z, Si J, Wang Q, et al. Highly efficient removal of methylene blue dye from an aqueous solution using cellulose acetate nanofibrous membranes modified by polydopamine. ACS Omega. 2020;5:5389–5400.
5. Sabar S, Abdul Aziz H, Yusof NH, Subramaniam S, Foo KY, Wilson LD, et al. Preparation of sulfonated chitosan for enhanced adsorption of methylene blue from aqueous solution. React Funct Polym. 2020;151:104584.
6. Staroń P, Chwastowski J, Banach M. Sorption behavior of methylene blue from aqueous solution by raphia fibers. Int J Environ Sci Technol. 2019;16:8449–8460.
7. Mabel M, Sundararaman TR, Parthasarathy N, Rajkumar J. Chitin beads from Peneaus sp. shells as a biosorbent for methylene blue dye removal. Pol J Environ Stud. 2019; 28(4):2253–9.

8. Cusioli LF, Quesada HB, Baptista ATA, Gomes RG, Bergamasco R. Soybean hulls as a low-cost biosorbent for removal of methylene blue contaminant. Environ Prog Sustain Energy. 2020;39:e13328.

9. Bhuyan MAH, Gebre RK, Finnilä MAJ, Illikainen M, Luukkonen T. Preparation of filter by alkali activation of blast furnace slag and its application for dye removal. J Environ Chem Eng. 2022;10:107051.

10. Hurairah SN, Lajis NM, Halim AA, Hurairah SN, Lajis NM, Halim A.A. Methylene blue removal from aqueous solution by adsorption on Archidendron jiringa seed shells. J Geosci Environ Prot. 2020;8:128–43.

11. Khan I, Saeed K, Zekker I, Zhang B, Hendi AH, Ahmad A, et al. Review on methylene blue: its properties, uses, toxicity and photodegradation. Water. 2022;14(2):242.

12. Sawant P, Parekar M, Kardile A, Khollam Y, Mene R. Exploring various experimental conditions for enhanced textile dye degradation using TiO2 as a photocatalyst. International e-Conference on Recent Trends in Material Science in Association with International Journal of Scientific Research in Science and Technology. Int J Sci Res Sci Technol. 2023;11(9):185–98.

13. Mirzaeifard Z, Shariatinia Z, Jourshabani M, Rezaei Darvishi SM. ZnO photocatalyst revisited: effective photocatalytic degradation of emerging contaminants using s-doped ZnO nanoparticles under visible light radiation. Ind Eng Chem Res. 2020;59:15894–911.

14. Rocha RLP, Honorio LMC, Silva-Filho EC, Osajima JA, Rocha RLP, Bezerra RDDS, et al. Light-activated hydroxyapatite photocatalysts: new environmentally-friendly materials to mitigate pollutants. Minerals. 2022;12:525.

15. Anandan D, Jaiswal AK. Synthesis methods of hydroxyapatite and biomedical applications: an updated review. J Aust Ceram Soc. 2023;60:663–79.

16. Nishikawa H, Omamiuda K. Photocatalytic activity of hydroxyapatite for methyl mercaptane. J Mol Catal A Chem. 2002;179:193–200.

17. Tsukada M, Wakamura M, Yoshida N, Watanabe T. Band gap and photocatalytic properties of Ti-substituted hydroxyapatite: comparison with anatase-TiO2. J Mol Catal A Chem. 2011;338:18–23.

18. Nishikawa H. Photo-induced catalytic activity of hydroxyapatite based on photo-excitation. Phosphorus Res Bull. 2007; 21:97–102.

19. Tripathi RM, Kumar N, Singh Bhadwal A, Gupta RK, Shrivastav BR, Shrivastav A. Facile and rapid biomimetic approach for synthesis of HAp nanofibers and evaluation of their photocatalytic activity. Mater Lett. 2015;140:64–7.

20. Tanaka H, Tsuda E, Nishikawa H, Fuji M. FTIR studies of adsorption and photocatalytic decomposition under UV irradiation of dimethyl sulfide on calcium hydroxyapatite. Adv Powder Technol. 2012;23:115–9.

21. Piccirillo C, Dunnill CW, Pullar RC, Tobaldi DM, Labrincha JA, Parkin IP, et al. Calcium phosphate-based materials of natural origin showing photocatalytic activity. J Mater Chem A Mater. 2013;1:6452–61.

22. Liu W, Qian G, Liu L, Fan X, Cai X, Feng J, et al. The growth mechanism of titania/hydroxyapatite and its application in the photodegradation of methyl orange dye under UV irradiation. Results Phys. 2018;11:112–7.

23. Golshan M, Zare M, Goudarzi G, Abtahi M, Babaei AA. Fe3O4@HAP-enhanced photocatalytic degradation of acid Red73 in aqueous suspension: optimization, kinetic, and mechanism studies. Mater Res Bull. 2017;91:59–67.

24. Othmani M, Bachoua H, Ghandour Y, Aissa A, Debbabi M. Synthesis, characterization and catalytic properties of copper-substituted hydroxyapatite nanocrystals. Mater Res Bull. 2018;97:560–6.

25. Mondal S, De Anda Reyes ME, Pal U. Plasmon induced enhanced photocatalytic activity of gold loaded hydroxyapatite nanoparticles for methylene blue degradation under visible light. RSC Adv. 2017;7:8633–45.

26. Chavan PN, Bahir MM, Mene RU, Mahabole MP, Khairnar RS. Study of nanobiomaterial hydroxyapatite in simulated body fluid: formation and growth of apatite. Mater Sci Eng B. 2010;168:224–30.

27. Costescu A, Ciobanu CS, Iconaru SL, Ghita RV, Chifiriuc CM, Marutescu LG, et al. Fabrication, characterization, and antimicrobial activity, evaluation of low silver concentrations in silver-doped hydroxyapatite nanoparticles. J Nanomater. 2013;2013:194854.

28. Mene RU, Mahabole MP, Mohite KC, Khairnar RS. Fe doped hydroxyapatite thick films modified via swift heavy ion irradiation for CO and CO_2 gas sensing application. J Alloys Compd. 2014;584:487–93.

29. Ciobanu CS, Iconaru SL, Le Coustumer P, Constantin LV, Predoi D. Antibacterial activity of silver-doped hydroxyapatite nanoparticles against gram-positive and gram-negative bacteria. Nanoscale Res Lett. 2012;7(1):324.

30. Yao J, Zhang Y, Wang Y, Chen M, Huang Y, Cao J, et al. Enhanced photocatalytic removal of NO over titania/hydro xyapatite (TiO2/HAp) composites with improved adsorption and charge mobility ability. RSC Adv. 2017;7:24683–9.

31. Ciobanu CS, Massuyeau F, Constantin LV, Predoi D. Structural and physical properties of antibacterial Ag-doped nano-hydroxyapatite synthesized at 100°C. Nanoscale Res Lett. 2011;6:1–8.

32. Iconaru SL, Chapon P, Le Coustumer P, Predoi D. Antimicrobial activity of thin solid films of silver doped hydroxyapatite prepared by sol-gel method. ScientificWorld Journal. 2014;2014:165351.

33. Ciobanu CS, Iconaru SL, Massuyeau F, Constantin LV, Costescu A, Predoi D. Synthesis, structure, and luminescent properties of europium-doped hydroxyapatite nanocrystalline powders. J Nanomater. 2012;2012:61.

34. Ciobanu CS, Iconaru SL, Le Coustumer P, Predoi D. Vibrational investigations of silver-doped hydroxyapatite with antibacterial properties. J Spectrosc. 2013;2013:471061.

35. Elsayed MS, Ahmed IA, Bader DMD, Hassan AF. Green synthesis of nano zinc oxide/nanohydroxyapatite composites using date palm pits extract and eggshells: adsorption

and photocatalytic degradation of methylene blue. Nanomaterials. 2022;12:49.

36. Qian J, Kang Y, Zhang W, Li Z. Fabrication, chemical composition change and phase evolution of biomorphic hydroxyapatite. J Mater Sci Mater Med. 2008;19:3373–83.
37. Elyacoubi A, Rkhaila A, Sallek B, El Idrissi BC. Antibacterial and photocatalytic performance of silver orthophosphate/hydroxyapatite composite. Mediterr J Chem. 2019;8:320–7.
38. Govindasamy P, Kandasamy B, Thangavelu P, Barathi S, Thandavarayan M, Shkir M, et al. Biowaste derived hydroxyapatite embedded on two-dimensional g-C3N4 nanosheets for degradation of hazardous dye and pharmacological drug via Z-scheme charge transfer. Sci Rep. 2022;12(1):1–16.
39. Shalan AE, Afifi M, El-Desoky MM, Ahmed MK. Electrospun nanofibrous membranes of cellulose acetate containing hydroxyapatite Co-doped with Ag/Fe: morphological features, antibacterial activity and degradation of methylene blue in aqueous solution. New J Chemistry. 2021;45:9212–20.
40. Elbasuney S, El-Khawaga AM, Elsayed MA, Elsaidy A, Correa-Duarte MA. Enhanced photocatalytic and antibacterial activities of novel Ag-HA bioceramic nanocatalyst for waste-water treatment. Sci Rep. 2023;13(1):1–15.
41. Hossain MS, Tuntun SM, Bahadur NM, Ahmed S. Enhancement of photocatalytic efficacy by exploiting copper doping in nano-hydroxyapatite for degradation of congo red dye. RSC Adv. 2022;12:34080–94.
42. Manoj M, Mangalaraj D, Meena P, Yuan A. Facile development and structural investigations of HAp and HAp/Ta nanostructures: photocatalytic activity against Turq blue GL dye. Mater Res Express. 2019;7:015012.
43. Hong X, Wu X, Zhang Q, Xiao M, Yang G, Qiu M, et al. Hydroxyapatite supported Ag_3PO_4 nanoparticles with higher visible light photocatalytic activity. Appl Surf Sci. 2012;258:4801–5.
44. Sheng G, Qiao L, Mou Y. Preparation of TiO2/hydrox yapatite composite and its photocatalytic degradation of methyl orange. J Environ Eng. 2011;137:611–6.
45. Mary I, Leethiyal R, Sekar P, Mangalaraj D, Viswanathan C, Ponpandian N. Self-assembly of nanostructured hydroxyapatite spheres for photodegradation of methylene blue dye. Mater Today Proc. 2019;18:1729–34.
46. Salhi A, Aarfane A, Tahiri S, Khamliche L, Bensitel M, Bentiss F, et al. Study of the photocatalytic degradation of methylene blue dye using titanium-doped hydroxyapatite. Mediterr J Chem. 2015;4(1):59–67.
47. Sha S, Zhang L, Liu H, Chen J, Che Y, Zhang F, Song C. Synthesis and visible-light photocatalytic degradation of Ag_3PO_4/AgBr/hydroxyapatite ternary nanocomposites prepared from oyster shells. RSC Adv. 2021;11(26):15598–607.
48. Guesmi Y, Agougui H, Lafi R, Jabli M, Hafiane A. Synthesis of hydroxyapatite-sodium alginate via a co-precipitation technique for efficient adsorption of methylene blue dye. J Mol Liq. 2018;249:912–20.
49. Dhatchayani S, Sankaranarayanan K, Kathiresan K. Tailoring of Ag_3PO_4-anchored hydroxyapatite nanophotocatalyst with tunable particle size by a facile ion-exchange method for organic textile dyes photodegradation. J Nanomater. 2023;2023:882964.
50. Enesca A, Isac L. The influence of light irradiation on the photocatalytic degradation of organic pollutants. Materials. 2020;13(11):2494.
51. Bouddouch A, Akhsassi B, Amaterz E, Bakiz B, Taoufyq A, Villain S, et al. Photodegradation under UV light irradiation of various types and systems of organic pollutants in the presence of a performant $BiPO_4$ photocatalyst. Catalysts. 2022;12:691.
52. Chahkandi M, Zargazi M, Ahmadi A, Koushki E, Ghasedi A. In situ synthesis of holey G-C3N4 nanosheets decorated by hydroxyapatite nanospheres as efficient visible light photocatalyst. RSC Adv. 2021;11:31174–88.
53. Anil K, Surenjan A. Green synthesis, characterisation, and performance evaluation of ZnO/TiO2 nanocomposite for cationic and anionic dye removal from aqueous solutions under solar irradiation. Water Pract Technol. 2024;19:824–38.
54. Lu L, Zhang Y, Yuan Z, Xu J, Li M, Wu Y, et al. Easily fabricated HARCP/HAp photocatalyst for efficient and fast removal of tetracycline under natural sunlight. Chem Eng J. 2021;412:128620.
55. Ha LPP, Vinh THT, Thuy NTB, Thi CM, Van Viet P. Visible-light-driven photocatalysis of anisotropic silver nanoparticles decorated on ZnO nanorods: synthesis and characterizations. J Environ Chem Eng. 2021;9:105103.
56. Lv S, Du Y, Wu F, Cai Y, Zhou T. Review on LSPR assisted photocatalysis: effects of physical fields and opportunities in multifield decoupling. Nanoscale Adv. 2022;4:2608–31.
57. Doan VD, Le VT, Le TTN, Nguyen HT. Nanosized zincated hydroxyapatite as a promising heterogeneous photo-fenton-like catalyst for methylene blue degradation. Adv Mater Sci Eng. 2019;2019:5978149.